



Photocatalytic degradation of 2,4,6-tribromophenol on Fe_2O_3 or FeOOH doped ZnIn_2S_4 heterostructure: Insight into degradation mechanism

Bo Gao, Lifen Liu*, Jiadong Liu, Fenglin Yang

Key Laboratory of Industrial Ecology and Environmental Engineering, MOE, School of Environmental, Science and Technology, Dalian University of Technology, Dalian 116024, PR China



ARTICLE INFO

Article history:

Received 5 July 2013

Received in revised form 7 September 2013

Accepted 22 September 2013

Available online 29 September 2013

Keywords:

Bromophenols

Semiconductor

Ferric oxide

Ferric hydroxide

Debromination

ABSTRACT

Taking advantage of the powerful photo-oxidation of iron (hydr)oxides and the outstanding reducing power of ZnIn_2S_4 , Fe_2O_3 or FeOOH doped ZnIn_2S_4 showed excellent photocatalytic activity in debromination of 2,4,6-tribromophenol (2,4,6-TBP). Though the FeOOH has great adsorption capacity, the Fe_2O_3 -doped ZnIn_2S_4 was found more active than FeOOH -doped ZnIn_2S_4 in mineralization of 2,4,6-tribromophenol. The addition of Fe_2O_3 or FeOOH narrowed the band gap of ZnIn_2S_4 . The degradation followed pseudo-first-order kinetics and the calculated overall photocatalytic degradation constants (K_f) of ZnIn_2S_4 , $\text{FeOOH-ZnIn}_2\text{S}_4$ and $\text{Fe}_2\text{O}_3-\text{ZnIn}_2\text{S}_4$ were 0.0499 min^{-1} , 0.0599 min^{-1} and 0.0861 min^{-1} under visible light illumination, and 0.35 min^{-1} , 1.52 min^{-1} and 1.59 min^{-1} under UV irradiation, respectively. After 2.0 h photocatalytic reaction on $\text{Fe}_2\text{O}_3-\text{ZnIn}_2\text{S}_4$ and $\text{FeOOH-ZnIn}_2\text{S}_4$, the released Br^- concentration was 26.3 mg l^{-1} and 23.8 mg l^{-1} corresponding 88% and 80% debromination, which was 1.41 and 1.28 times higher than the debromination by ZnIn_2S_4 , respectively. The tentative photocatalytic degradation pathways on $\text{Fe}_2\text{O}_3-\text{ZnIn}_2\text{S}_4$ and $\text{FeOOH-ZnIn}_2\text{S}_4$ were proposed based on the detected intermediates.

© 2013 Elsevier B.V. All rights reserved.

1. Introduction

Ternary sulfide ZnIn_2S_4 as the member of the AB_2X_4 semiconductor has been actively studied as an efficient visible-light-driven photocatalyst for hydrogen production [1,2] and inactivation of *E. coli* [3]. Hexagonal ZnIn_2S_4 microspheres and cubic ZnIn_2S_4 nanoparticles can be controllably synthesized and different polymorphs of ZnIn_2S_4 can exhibit different photocatalytic performance for dye degradation [4,5]. The ZnIn_2S_4 with a relative high conduction edge (-0.91 V versus NHE) [6] has shown to be a powerful reductant, while the valence band holes are less oxidizing, which might be detrimental to advanced oxidation and complete mineralization of pollutants.

Ferric oxide and hydroxide, widespread in natural environment, have a narrow band gap of $2.0\text{--}2.2 \text{ eV}$ and high absorbency in the visible-light range. Moreover, both ferric oxide and hydroxide have valence band edges $2\text{--}3 \text{ eV}$ below the H_2O oxidation potential which indicate strong photo-oxidation in aqueous solution. Iron oxides, on the other hand, are good alternatives for pollutants degradation under visible light because of their stability,

non-toxicity, simple production and abundance in nature. In fact, there have been several reports using Fe_2O_3 and FeOOH as photocatalyst for degradation of various pollutants such as chlorophenols [7] and dyes [8–10], 2,6-dimethylphenol [11] and 2-aminophenol [12], estrogen [13] and pesticides [14], polybromodiphenyl ethers [15]. However, the conduction band edges of Fe_2O_3 and FeOOH are below the H_2O reduction potential, which limit their reducing power. The photocatalytic efficiencies are limited because of the short lifetime of photo-excited carrier and short diffusion length for surface reactions and the fast electron/hole recombination [16]. Therefore, several kinds of materials such as metal Ru [17], metal oxide CuO [18] and semiconductors (TiO_2 [19], CdS [20] and WO_3 [21]) have been used as dopants to enhance the photocatalytic performance. Comparing with Fe_2O_3 , FeOOH showed excellent adsorption capacity due to its high surface area [22], and organic-goethite surface complex formation was involved in photocatalytic degradation of aromatic compounds at FeOOH surface [23].

In this paper, semiconductor Fe_2O_3 and FeOOH were used as dopants and integrated with ternary semiconductor ZnIn_2S_4 . Taking advantage of the different energy band structure of semiconductors, the build-in internal electric field can prompt the reverse movement of photo-induced electrons and holes, and further realize the effective separation of excited electrons and holes. It is anticipated that the outstanding reducing power of

Abbreviation: 2,4,6-TBP, 2,4,6-tribromophenol.

* Corresponding author. Tel.: +86 411 84706173; fax: +86 411 84708083.

E-mail addresses: gblj1986@163.com (B. Gao), estdlut@foxmail.com (L. Liu).

ZnIn_2S_4 assisted with the powerful photo-oxidation of Fe_2O_3 or FeOOH could improve the photocatalytic degradation rate of 2,4,6-tribromophenol, photocatalytic debromination and mineralization efficiency. The distinctive photocatalytic reaction mechanism of FeOOH may play an important role in the debromination mechanism of the composite FeOOH -doped ZnIn_2S_4 . The possible debromination mechanism on Fe_2O_3 - ZnIn_2S_4 and FeOOH - ZnIn_2S_4 were proposed and compared.

2. Experiment

2.1. Chemicals

2,4,6-Tribromophenol (AR) was supplied by Sinpharm Chemical Reagent Co., Ltd. The initial concentration of 2,4,6-TBP was 0.124 mM and the initial pH was 6.13. Other reagents such as $\text{Zn}(\text{NO}_3)_2 \cdot 6\text{H}_2\text{O}$, $\text{In}(\text{NO}_3)_3 \cdot 5\text{H}_2\text{O}$, CH_3CSNH_2 (TAA), $\text{FeSO}_4 \cdot 7\text{H}_2\text{O}$, $\text{FeCl}_3 \cdot 6\text{H}_2\text{O}$, NaOH , Na_2CO_3 and EDTA were of analytical grade. All materials were used as received without further purification. The water used in this test was ultrapure water.

2.2. Preparation of Fe_2O_3 , FeOOH , ZnIn_2S_4 , Fe_2O_3 - ZnIn_2S_4 and FeOOH - ZnIn_2S_4

Fe_2O_3 was prepared according to previous research [24], 100 ml of 3 M NaOH was added drop wise to 400 ml of 0.2 M $\text{FeCl}_3 \cdot 6\text{H}_2\text{O}$ aqueous solution under magnetic stirring at room temperature. After stirring 1.5 h, the precipitate was separated by centrifugation at 10,000 rpm for 5 min, and then washed with deionized water several times until there was no white precipitate generated when adding 0.05 M AgNO_3 solution. The solid precipitate was ground to powders after being dried at 60 °C in vacuum for 10 h and then sintered in the electric muffle furnace at 300 °C for 2.0 h. The particles were sieved through 320 mesh sieve.

FeOOH was prepared in a simple procedure, 15 ml Na_2CO_3 saturated solution was added into 55 ml 0.3 M $\text{FeSO}_4 \cdot 7\text{H}_2\text{O}$ solution drop by drop under vigorously stirring in 20 °C water bath and white-green precipitate was generally formed. Next, 5 ml 0.015 M EDTA solution was slowly added to the mixture. The resulting mixture was purged with high purity oxygen at a flow of 1.0 l min⁻¹ for 30 min. Along with the flow of oxygen, the color of the precipitate was generally getting darker which changed from white-green to blue-green and finally changed to dark red-brown. The precipitate was washed with deionized water until the solution was neutral and there was no impurity ionic existed. Then the FeOOH precipitate was dried at 60 °C under vacuum and stored after milling and sieving through 320 mesh sieve.

ZnIn_2S_4 , Fe_2O_3 - ZnIn_2S_4 and FeOOH - ZnIn_2S_4 were synthesized in a typical hydrothermal procedure, 0.5 mmol $\text{Zn}(\text{NO}_3)_2 \cdot 6\text{H}_2\text{O}$ and 1.0 mmol $\text{In}(\text{NO}_3)_3 \cdot 5\text{H}_2\text{O}$ and an excessive CH_3CSNH_2 (TAA, 8 mmol) were dissolved in 100 ml deionized water (solution A) and then transferred to a 120 ml Teflon-lined autoclave. The autoclave was sealed and maintained under magnetic stirring at 80 °C for 6.0 h and then allowed to cool to ambient temperature naturally. The yellow ZnIn_2S_4 product was obtained by centrifugation at 10,000 rpm for 5 min, and then washed twice with deionized water and finally dried in vacuum at 60 °C. For the synthesis of Fe_2O_3 - ZnIn_2S_4 and FeOOH - ZnIn_2S_4 , a desired amount of prepared Fe_2O_3 or FeOOH powder was added into the mixture (solution A) before transferring into the autoclave. Different amounts of Fe_2O_3 or FeOOH doped ZnIn_2S_4 was denoted as Fe_2O_3 (X)- ZnIn_2S_4 or FeOOH (X)- ZnIn_2S_4 , where the value of X (5%, 10% and 15%) represented the weight content of Fe_2O_3 or FeOOH versus the weight content of ZnIn_2S_4 .

2.3. Experimental setup

The visible light and UV-light photocatalytic degradation of 2,4,6-TBP were conducted in an aqueous solution at room temperature. The UV-light photocatalytic reactor was a cylindrical quartz tube with a dimension of 3 cm × 30 cm (diameter × height). The UV light source was a 20 W germicidal low-pressure mercury lamp with main wavelength of 254 nm. A glass cooling thimble with 3 cm inner diameter and 30 cm height was used as visible light photocatalytic reactor. A 100 W Tungsten-Halogen filtered after a hard glass (main emission from 420 nm to 2000 nm) was applied as visible light source. The distance between reactor and lamp was 14 cm. The light intensity of UV-light and visible light was 250 $\mu\text{W cm}^{-2}$ and 1554 mW cm^{-2} (with Al reflector surrounding the reactor and the lamp), respectively, 14 cm away from the lamp, measured by a UVA radiometer. A 0.5 g l⁻¹ catalyst dosage was applied in this research and aeration (0.11 min⁻¹) was applied for thorough mixing and suspension. 5 ml reaction suspension was withdrawn at specific time intervals and filtered through 0.22 μm millipore (acetate cellulose) filter for further analysis.

2.4. Experiment for determining the photocatalysis and debromination mechanism

Isopropanol had been described as the most effective hydroxyl radical scavenger [14]. Therefore, isopropanol was used to determine whether if there was hydroxyl radical formed in the solution. 50 mg of Fe_2O_3 (10%)- ZnIn_2S_4 and/or FeOOH (10%)- ZnIn_2S_4 and 2 ml isopropanol were dispersed in 100 ml 2,4,6-TBP solution. And the experiment without isopropanol was conducted as a comparison. Phosphate was proved effective in ligand exchange of surface hydroxyl groups on FeOOH [25]. 50 mg FeOOH (10%)- ZnIn_2S_4 was dispersed in 10 ml 10 mM KH_2PO_4 solution. After magnetic stirring for 12 h, the samples were separated by centrifugation at 10,000 rpm for 5 min and the collected precipitate was phosphate bound catalyst. Then the phosphate bound FeOOH (10%)- ZnIn_2S_4 was applied to degrade 2,4,6-TBP under UV irradiation.

2.5. Photocatalyst stability study

25 mg Fe_2O_3 (10%)- ZnIn_2S_4 or FeOOH (10%)- ZnIn_2S_4 photocatalyst was added into 50 ml of 2,4,6-TBP solution and then irradiated under UV light for 2.0 h. After the 1st 2.0 h photocatalytic reaction, the mixture was centrifuged at 12,000 rpm for 5 min to recover the suspended catalysts. Then the collected photocatalysts (Fe_2O_3 - ZnIn_2S_4 or FeOOH - ZnIn_2S_4) were dispersed in 50 ml fresh 2,4,6-TBP solution to carry out the second test. The supernatant was used to analyze the concentration of 2,4,6-TBP, bromide ion content and COD_{Mn} content. In this way, the experiments were repeated for 9 times. When the 10th cyclic experiment was completed, the catalyst was collected and dried at 60 °C in a vacuum. After being dried, the catalyst was weighed to measure the loss of catalyst in the cyclic experiment.

2.6. Analysis and characterization

The concentration of 2,4,6-TBP was determined by high performance liquid chromatography (HPLC, Shimadzu, VP-ODS, 150 L × 4.6). The mobile phase was 80% methanol and 20% water with a flow rate of 1.0 ml min⁻¹. An injection volume of 5 μl was used and the UV detector wavelength was set at 295 nm. The extent of mineralization of 2,4,6-TBP was measured by reduced COD_{Mn} according to the standard methods for the examination of water and wastewater (American Public Health Association, 2005). The released Br⁻ was measured according to the method for determining bromide content in groundwater (F-HZ-DZ-DXS-0062, China).

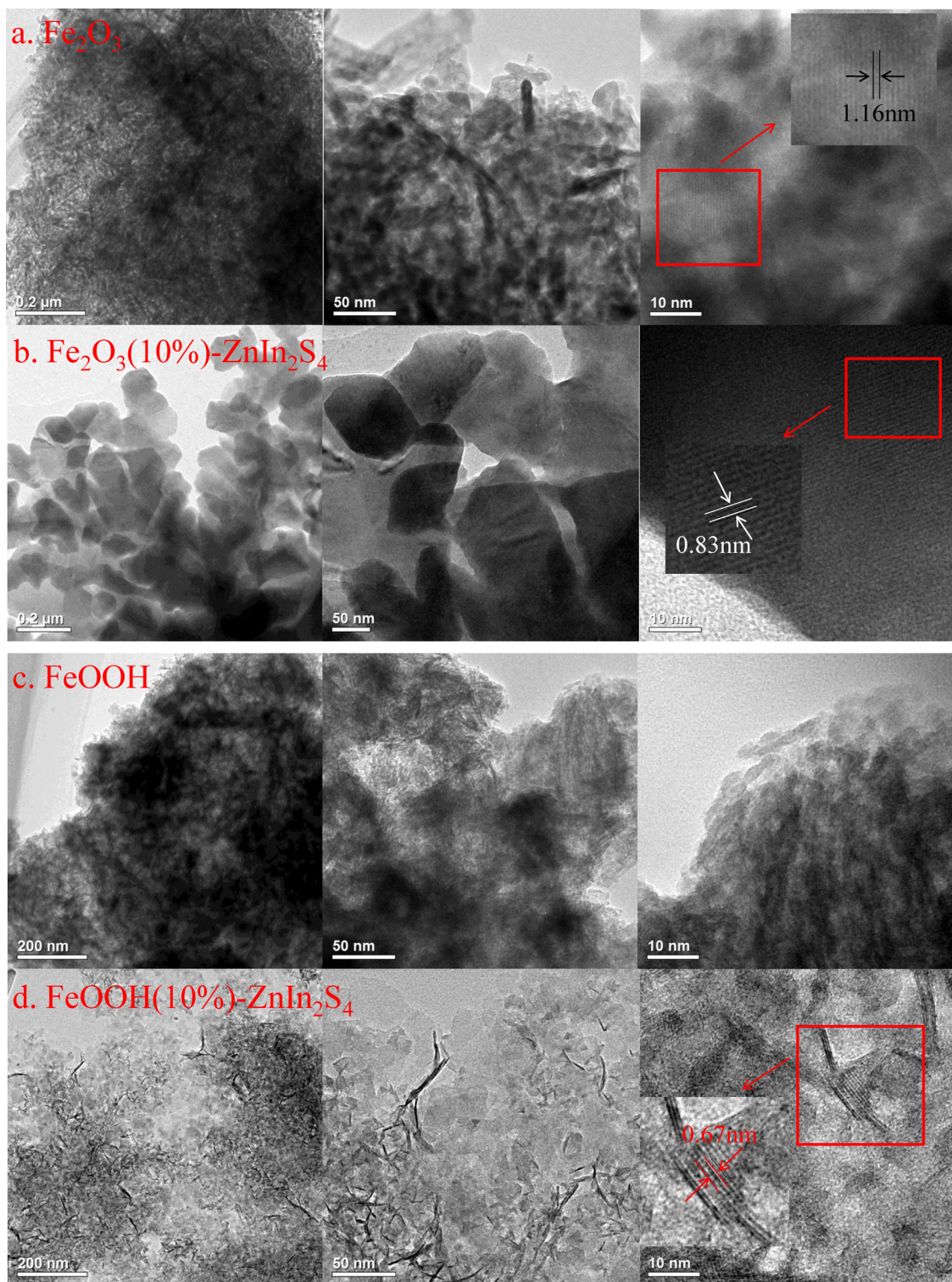


Fig. 1. TEM images of Fe_2O_3 (a), Fe_2O_3 (10%)- ZnIn_2S_4 (b), FeOOH (c) and FeOOH (10%)- ZnIn_2S_4 (d).

The molecular masses of 2,4,6-TBP and its potential intermediates were determined in the negative mode by the liquid chromatography-electron spray ionization mass spectrometry (LC-ESI-MS, Agilent Technologies). The mobile phase was a mixture of 50% ultrapure water supplemented with 0.2% formic acid and 50% acetonitrile with a flow rate of 0.25 ml min^{-1} . 5 μl of the extracted samples were injected and detector wavelength was set at 295 nm.

Transmission electron microscopy (TEM-100CX-II) analyses were operated at an accelerating voltage of 200 kV. The crystal structures of the particles were characterized by powder X-ray diffraction (XRD) using $\text{Cu K}\alpha$ ($\lambda = 1.5406 \text{ \AA}$) radiation at a scanning speed of 4° min^{-1} ranging from 10° to 80° . The accelerating voltage and applied current were 40 kV and 100 mA, respectively. The optical properties of the prepared samples were measured by a UV-Vis spectrophotometer (JASCO Corp., V-550).

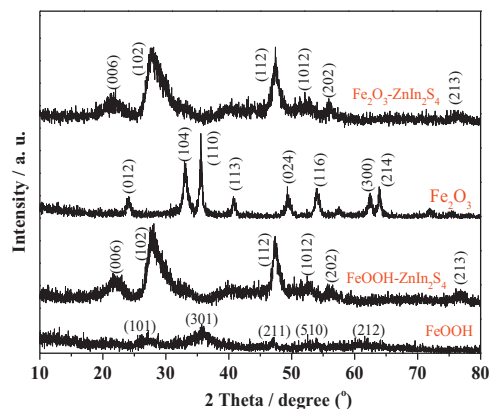


Fig. 2. XRD patterns of the as-prepared FeOOH, Fe_2O_3 , FeOOH (10%)– ZnIn_2S_4 and Fe_2O_3 (10%)– ZnIn_2S_4 .

3. Results and discussion

3.1. Characterization

As shown in Fig. 1 a, rod shape particles with an average diameter of 6–8 nm and a length of ~50 nm were observed in the Fe_2O_3 aggregates. The lattice interplanar spacing measured from the HRTEM image of Fe_2O_3 was 1.16 nm. The morphology of Fe_2O_3 (10%)–doped ZnIn_2S_4 (Fig. 1b) was shown by majority of irregular amorphous blocky structures (average width of ~200 nm and length of ~260 nm) and minority of rod structures which might be related to the doping Fe_2O_3 . Comparing with the microsphere morphology of ZnIn_2S_4 (average diameter 2–4 μm) reported in our previous research [26], the blocky structure of Fe_2O_3 -doped ZnIn_2S_4 was much smaller. The lattice interlayer distance was measured to be ~0.83 nm.

The TEM image of FeOOH (Fig. 1c) presented some needle-like structures of various lengths with an average diameter of ~2 nm, which was consistent with α -FeOOH structure in literature [27]. The HRTEM image was not clear enough to measure the lattice interplanar distance due to the strong magnetic interference of FeOOH. After doping with ZnIn_2S_4 , the composite was comprised of some amorphous blocks and some nanofiber structures (Fig. 1d). The needle-like fiber can be regarded as FeOOH, which demonstrated that FeOOH was doped with ZnIn_2S_4 successfully. The lattice interplanar spacing of FeOOH doped ZnIn_2S_4 was measured to be 0.67 nm.

The XRD patterns of Fe_2O_3 , FeOOH, Fe_2O_3 (10%)– ZnIn_2S_4 and FeOOH (10%)– ZnIn_2S_4 samples were shown in Fig. 2. All the diffraction peaks of the obtained FeOOH and Fe_2O_3 can be indexed as the reflection of α -FeOOH [27] and α - Fe_2O_3 [28]. The XRD patterns of composite $\text{Fe}_2\text{O}_3\text{-ZnIn}_2\text{S}_4$ and FeOOH– ZnIn_2S_4 mainly revealed diffraction peaks of ZnIn_2S_4 . The characteristic diffraction peaks of FeOOH and Fe_2O_3 were not observed in the composite XRD patterns, which indicated that the doped Fe_2O_3 or FeOOH did not incorporate into the lattice of the ZnIn_2S_4 and the composites might be formed by the physical bond between ZnIn_2S_4 and Fe_2O_3 or FeOOH.

Fig. 3 showed the UV-vis diffuse reflectance spectrum of prepared Fe_2O_3 , FeOOH, ZnIn_2S_4 , $\text{Fe}_2\text{O}_3\text{-ZnIn}_2\text{S}_4$ and FeOOH– ZnIn_2S_4 powders. FeOOH and Fe_2O_3 samples had high intensity and wide absorbency ranged from UV to visible region (Fig. 3a). The onset of the absorption edge of ZnIn_2S_4 was at 580–600 nm. The absorption edge of composite FeOOH-doped ZnIn_2S_4 and Fe_2O_3 -doped ZnIn_2S_4 red-shifted slightly comparing with ZnIn_2S_4 . The band gap (E_g) can be evaluated according to the following formula [29]

$$(\alpha h\nu)^n = A(h\nu - E_g) \quad (1)$$

where α , $h\nu$, E_g , A were the absorption coefficient, the photon energy, the band gap energy and a constant, respectively. The value of n corresponded to 1/2, 2, 3/2 and 3 for allowed direct, allowed indirect, forbidden direct and forbidden indirect transitions, respectively [30]. A classical extrapolation approach was applied to estimate the band gaps (E_g) of prepared samples by plotting $(\alpha h\nu)^{1/n}$ with respect to $h\nu$. The plot of $(\alpha h\nu)^{1/2}$ versus $h\nu$ based on the indirect-allowed transition [30] of ZnIn_2S_4 was shown in Fig. 3b. Extrapolating the straight line to the photon energy axis, the band gap energy of ZnIn_2S_4 was 2.0 eV. The addition of Fe_2O_3 and/or FeOOH narrowed the band gap and the band gaps of FeOOH-doped ZnIn_2S_4 and Fe_2O_3 -doped ZnIn_2S_4 calculated in this way were 1.85 eV and 1.75 eV, respectively. According to allowed direct optical transition [31], the band gaps of FeOOH and Fe_2O_3 determined by plotting $(\alpha h\nu)^2$ versus $h\nu$ were 1.85 eV and 1.78 eV, respectively (Fig. 3c).

3.2. Adsorption of 2,4,6-tribromophenol

Dark control experiments were carried out to evaluate the adsorption properties of as-prepared samples. Fig. 4 showed the adsorption removal of 2,4,6-TBP by Fe_2O_3 (X)- ZnIn_2S_4 and FeOOH (X)- ZnIn_2S_4 (X =0%, 5%, 10% and 15%). The pure ZnIn_2S_4 without doping Fe_2O_3 or FeOOH represented excellent adsorption performance and 92% 2,4,6-TBP was removed after 2.0 h adsorption in the dark. No obvious removal of 2,4,6-TBP (16%) was observed after 2.0 h adsorption by Fe_2O_3 . Comparing with the poor adsorption performance of Fe_2O_3 , FeOOH showed much better adsorption of 2,4,6-TBP in the dark and 67% 2,4,6-TBP was removed. When ZnIn_2S_4 was doped with Fe_2O_3 , the adsorption capacity of Fe_2O_3 (X)- ZnIn_2S_4 was decreased a lot from 92% to 52% with the amount of Fe_2O_3 doped increasing from 0% to 15%, which was due to the poor adsorption of Fe_2O_3 . Increasing the doped amount of FeOOH also led to gradual decrease in the adsorption capacity of FeOOH (X)- ZnIn_2S_4 , but there was a tiny difference (82–87%), which was better than FeOOH but not as good as ZnIn_2S_4 . Both FeOOH and ZnIn_2S_4 showed good adsorption performance, so doping a small amount of FeOOH can slightly affect the adsorption capacity of ZnIn_2S_4 .

3.3. Photocatalytic degradation of 2,4,6-tribromophenol

3.3.1. Degradation of 2,4,6-tribromophenol under visible light

The prepared $\text{Fe}_2\text{O}_3\text{-ZnIn}_2\text{S}_4$ and FeOOH– ZnIn_2S_4 both have a broad visible light absorbency, so the photocatalytic degradation of 2,4,6-TBP was studied using visible light. Though the adsorption capacity of $\text{Fe}_2\text{O}_3\text{-ZnIn}_2\text{S}_4$ is much less than ZnIn_2S_4 and FeOOH– ZnIn_2S_4 , $\text{Fe}_2\text{O}_3\text{-ZnIn}_2\text{S}_4$ displayed the best photocatalytic activity under visible light. This indicated that adsorption was not a major factor affecting photocatalytic activity.

The degradation of 2,4,6-TBP under visible light and UV light can be described by pseudo-first-order rate equation:

$$\frac{dC}{dt} = -K_r C \quad (2)$$

where "C" is the aqueous phase concentration of 2,4,6-TBP (mg l^{-1}). " K_r " is the pseudo-first-order rate constant (min^{-1}) which can be determined by plotting $\ln(C_t/C_0)$ versus reaction time t (min). At the start of photocatalytic reaction, the substrate concentration was marked as C_0 . As shown in Fig. 5, it took 60 min, 80 min and 100 min for complete removal of 2,4,6-TBP under visible light by $\text{Fe}_2\text{O}_3\text{-ZnIn}_2\text{S}_4$, FeOOH– ZnIn_2S_4 and ZnIn_2S_4 , respectively. For the first 50 min, the reaction of ZnIn_2S_4 was faster than FeOOH– ZnIn_2S_4 , but the overall pseudo-first-order rate constant was smaller than FeOOH– ZnIn_2S_4 . The pseudo-first-order rate constants for degradation of 2,4,6-TBP under visible light by

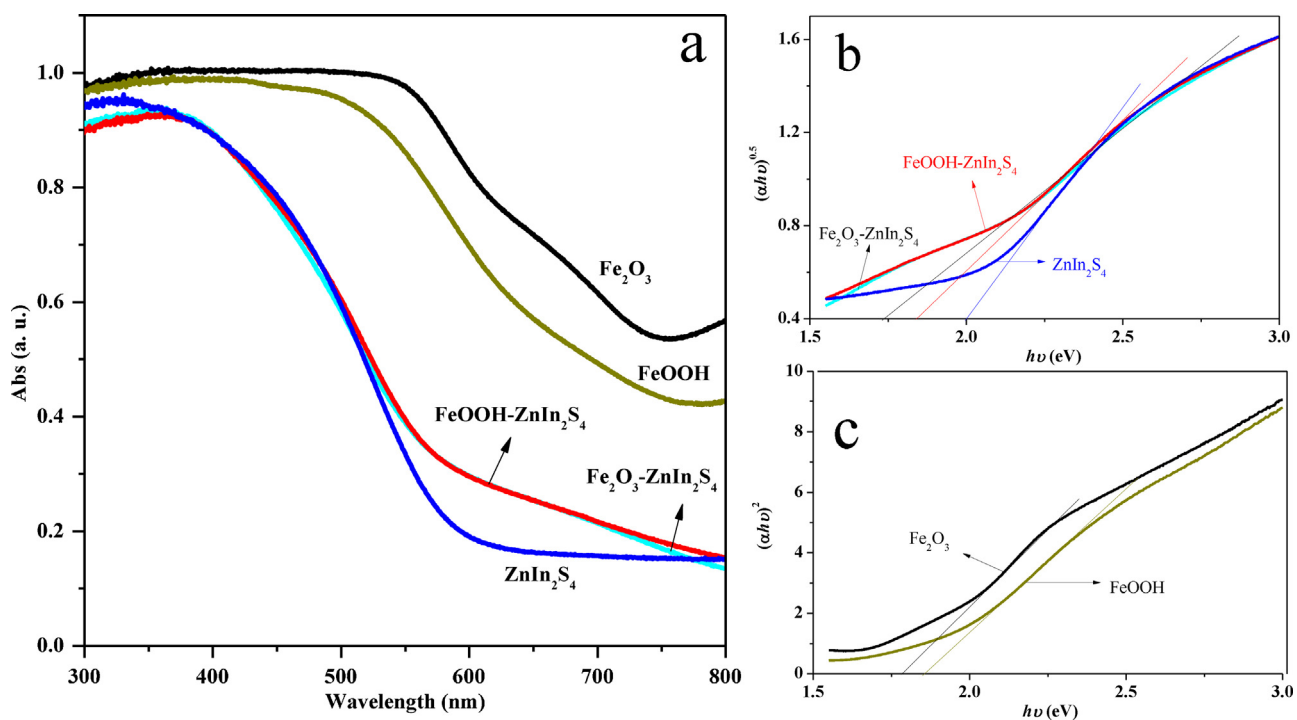


Fig. 3. (a) UV-vis diffuse reflectance spectra of Fe_2O_3 , FeOOH , $\text{FeOOH-ZnIn}_2\text{S}_4$, $\text{Fe}_2\text{O}_3-\text{ZnIn}_2\text{S}_4$ and ZnIn_2S_4 . (b) Plots of $(\alpha h\nu)^{0.5}$ versus photon energy ($h\nu$). (c) Plots of $(\alpha h\nu)^2$ versus photon energy ($h\nu$).

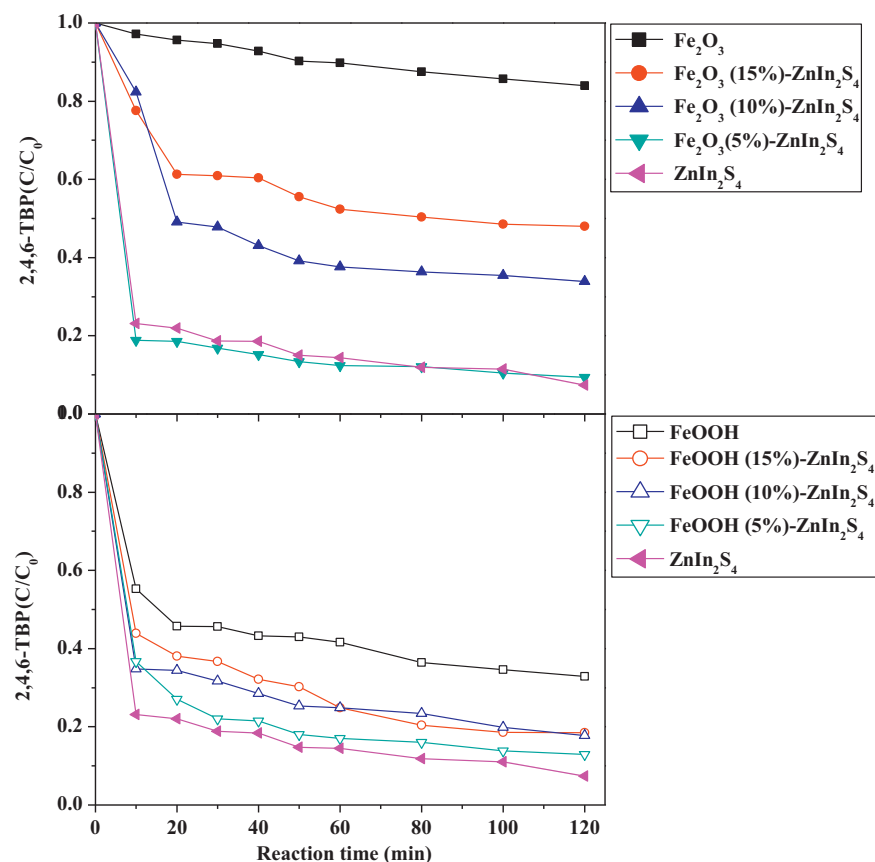


Fig. 4. The adsorption removal of 2,4,6-TBP in the dark.

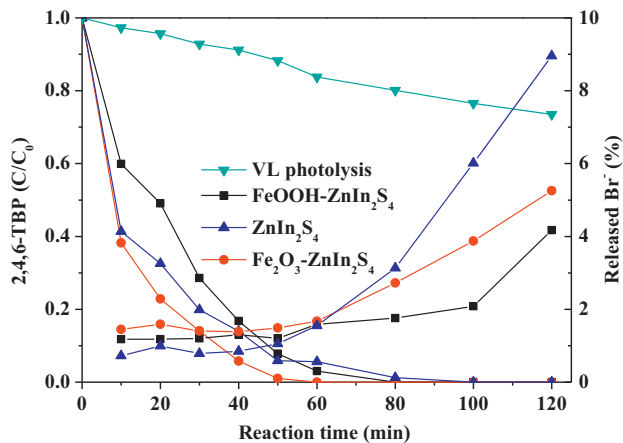


Fig. 5. Photodegradation of 2,4,6-TBP and the relative released Br^- under visible light.

ZnIn₂S₄, FeOOH-ZnIn₂S₄ and Fe₂O₃-ZnIn₂S₄ were 0.0499 min^{-1} , 0.0599 min^{-1} and 0.0861 min^{-1} , respectively (Table S1).

The C/C_{100} ratio of Br^- was used to evaluate the debromination efficiency. C_{100} of bromide was defined as the Br^- concentration at 100% debromination and C represented the released bromide concentration. Comparing with the changes in rate constants, the debromination tendency was the opposite and ZnIn₂S₄ showed the best debromination efficiency. This might be related to the different debromination pathway by ZnIn₂S₄ and Fe₂O₃-ZnIn₂S₄. The potential value of ZnIn₂S₄ conduction band is negative enough (-0.91 V versus NHE) to reduce the surface chemisorbed O_2 to yield the strong oxidizing species $\text{O}_2^{\bullet-}$ ($E^\circ(\text{O}_2/\text{O}_2^{\bullet-}) = -0.33 \text{ V}$ versus NHE) [4]. Also, the electrons would transfer to 2,4,6-TBP adsorbed on the surface of ZnIn₂S₄ for reductive debromination. The valence band hole of Fe₂O₃ was shown to be a powerful oxidant [7]. When the Fe₂O₃-doped ZnIn₂S₄ was illuminated by visible light, the electron would transfer from the conduction band of ZnIn₂S₄ to the conduction band of Fe₂O₃. During the charge transfer process, a portion of energy will be lost, which will result in some reduction of redox ability. The oxidative reaction by photo-induced holes played a leading role in degradation of 2,4,6-TBP to produce quinones intermediates and then further debromination. That's the reason that the removal rate of 2,4,6-TBP was faster by Fe₂O₃-ZnIn₂S₄, while the debromination efficiency was higher by ZnIn₂S₄. But the overall debromination efficiency was very low (lower than 10%), which did not meet the intended purpose to reduce the toxicity of 2,4,6-TBP. In order to reduce the toxic by-products and realize mineralization, a 20 W germicidal low-pressure mercury lamp was applied in the subsequent experiments.

3.3.2. Degradation of 2,4,6-tribromophenol under UV light

Control tests for photocatalytic degradation of 2,4,6-TBP under UV illumination by ZnIn₂S₄ and different content of Fe₂O₃ or FeOOH doping ZnIn₂S₄ were conducted. Pollutant 2,4,6-TBP can be easily transformed to quinones intermediates and 2,4,6-TBP was eliminated after 1.0 h in the presence of UV irradiation. As shown in Fig. 6, 2,4,6-TBP disappeared much more rapidly in the presence of photocatalysts. From the partial enlarged view (inset in Fig. 6), 2,4,6-TBP was not detected after 6 min irradiation in the reaction system containing Fe₂O₃-ZnIn₂S₄, FeOOH or FeOOH-ZnIn₂S₄, and also 2,4,6-TBP completely disappeared after 8 min irradiation in the presence of ZnIn₂S₄ or Fe₂O₃. The degradation rates were influenced by the amount of Fe₂O₃ or FeOOH doping. Fe₂O₃-ZnIn₂S₄ or FeOOH-ZnIn₂S₄ exhibited outstanding photocatalytic activity when the amount of doped Fe₂O₃ or FeOOH was 10 wt%. The pseudo-first-order rate constants (Table

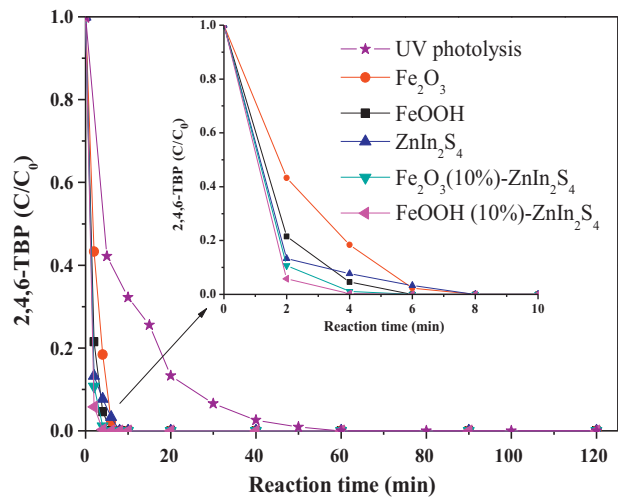


Fig. 6. Photodegradation of 2,4,6-TBP under UV irradiation (Inset is the photodegradation of 2,4,6-TBP in 10 min).

S1) can clearly reveal the difference in the degradation kinetics of 2,4,6-TBP on different photocatalysts, which showed that the overall photocatalytic degradation increased in the order of ZnIn₂S₄ (0.35 min^{-1}) < Fe₂O₃ (0.71 min^{-1}) < FeOOH (0.77 min^{-1}) < FeOOH (10%)-ZnIn₂S₄ (1.52 min^{-1}) < Fe₂O₃ (10%)-ZnIn₂S₄ (1.59 min^{-1}).

However, after 2.0 h photocatalytic reaction, the debromination efficiency was in the order of FeOOH (44%) < Fe₂O₃ (55%) < ZnIn₂S₄ (63%) < FeOOH-ZnIn₂S₄ (80%) < Fe₂O₃-ZnIn₂S₄ (88%), which was a little different from photocatalytic degradation rate. Doping Fe₂O₃ and/or FeOOH with ZnIn₂S₄ not only accelerated the photocatalytic degradation rate but also improved the debromination efficiency (Fig. 7). The debromination efficiencies were barely influenced by the doping content of Fe₂O₃ or FeOOH. After 2.0 h photocatalytic reaction on Fe₂O₃-ZnIn₂S₄ and FeOOH-ZnIn₂S₄, the released Br^- concentration was 26.3 mg l^{-1} and 23.8 mg l^{-1} corresponding 88% and 80% debromination, which was 1.41 and 1.28 times higher than the debromination by ZnIn₂S₄, respectively. Fe₂O₃ was integrated with ZnIn₂S₄ as a powerful oxidant can enhance the oxidative debromination and also can transfer the conduction band electrons of ZnIn₂S₄ immediately to reduce the recombination of electrons and holes.

Mineralization is the ultimate purpose of photocatalytic degradation of 2,4,6-TBP, so COD_{Mn} was measured after 2.0 h reaction to evaluate the mineralization degree. Though the degradation rate and debromination efficiency were enhanced by FeOOH-doped ZnIn₂S₄, the COD_{Mn} removal was not improved. While, as shown in Fig. 8, 72% COD_{Mn} removal was achieved by Fe₂O₃-doped ZnIn₂S₄, which was improved 16% comparing with COD_{Mn} removal by ZnIn₂S₄. According to the degradation rate, debromination and mineralization efficiency, Fe₂O₃-doped ZnIn₂S₄ exhibited better photocatalytic activity than FeOOH-doped ZnIn₂S₄. The photocatalytic debromination mechanism was discussed in the following section.

3.4. Debromination pathways analysis

The intermediate products resulting from 2,4,6-TBP photocatalytic degradation by Fe₂O₃/ZnIn₂S₄ and FeOOH/ZnIn₂S₄ under UV irradiation at 10 min and 60 min were analyzed using HPLC-ESI-MS. 2,4,6-TBP was completely decomposed and subsequently degraded to simpler compounds, even leading to complete mineralization. According to the LC-MS analysis, five intermediate products corresponding to mass spectrum at *m/z* 346.8, 296.7, 266.8, 250.8 and 187 were detected after 10 min

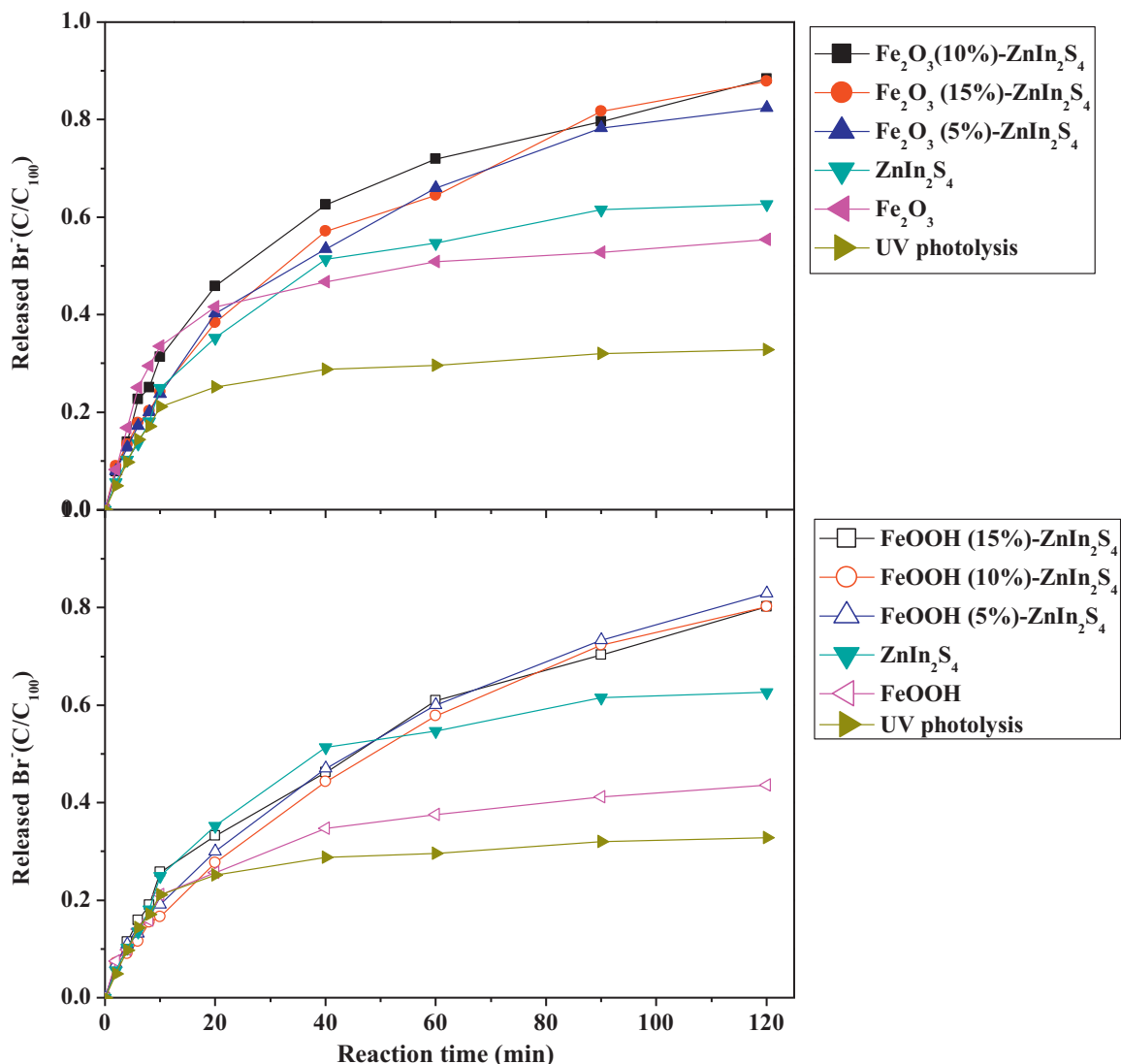


Fig. 7. The released Br[−] concentration (C_{100} of bromide was determined as the Br[−] concentration at 100% debromination and C represented the released bromide concentration).

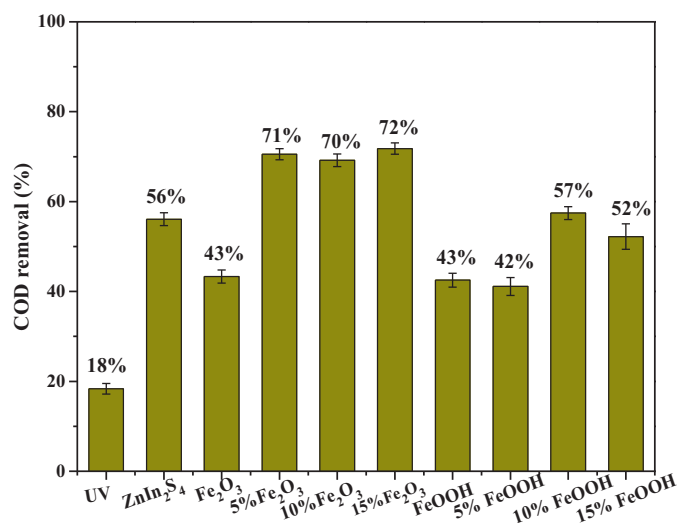


Fig. 8. COD_{MN} removal rates for 2,4,6-TBP by different photocatalysts after 2.0 h reaction ($[2,4,6\text{-TBP}]_0 = 0.124 \text{ mM}$, pH 6.13, catalyst dosage = 0.5 g l^{-1} , 20 W low-pressure mercury lamp (light intensity was $250 \mu\text{W cm}^{-2}$)).

photocatalytic debromination on Fe₂O₃/ZnIn₂S₄ (Fig. 9A). After 60 min reaction, seven new intermediates (m/z 330, 304.7, 280.8, 222.8, 207.8, 159 and 110) were detected (Fig. 9B). With regard to FeOOH/ZnIn₂S₄, the same five intermediates were also detected after 10 min reaction (Fig. 9C), but there was no new intermediate appeared after 60 min reaction (Fig. 9D). The relative intensity of 2,6-dibromo-P-benzoquinone decreased and 2-bromo-1,4-benzoquinone increased within 60 min photocatalytic reaction on FeOOH-ZnIn₂S₄ (Fig. S2). This attributed that 2,6-dibromo-P-benzoquinone was further degraded and resulted in the accumulation of 2-bromo-1,4-benzoquinone. The intermediates were decomposed immediately on Fe₂O₃-doped ZnIn₂S₄ (Fig. S2), which explained that the mineralization efficiency on Fe₂O₃-ZnIn₂S₄ was higher than FeOOH/ZnIn₂S₄ and further confirmed that Fe₂O₃/ZnIn₂S₄ exhibited better photocatalytic activity than FeOOH/ZnIn₂S₄.

According to the LC-MS results in this study, the photodegradation pathway of 2,4,6-TBP was proposed in Scheme 1. Four main degradation pathways were involved in the photocatalytic degradation of 2,4,6-TBP on Fe₂O₃/ZnIn₂S₄. The first pathway (marked as (1)) was the hydroxylation process of benzene ring. The second one (marked as (2)) was substitution reaction of bromide in benzene

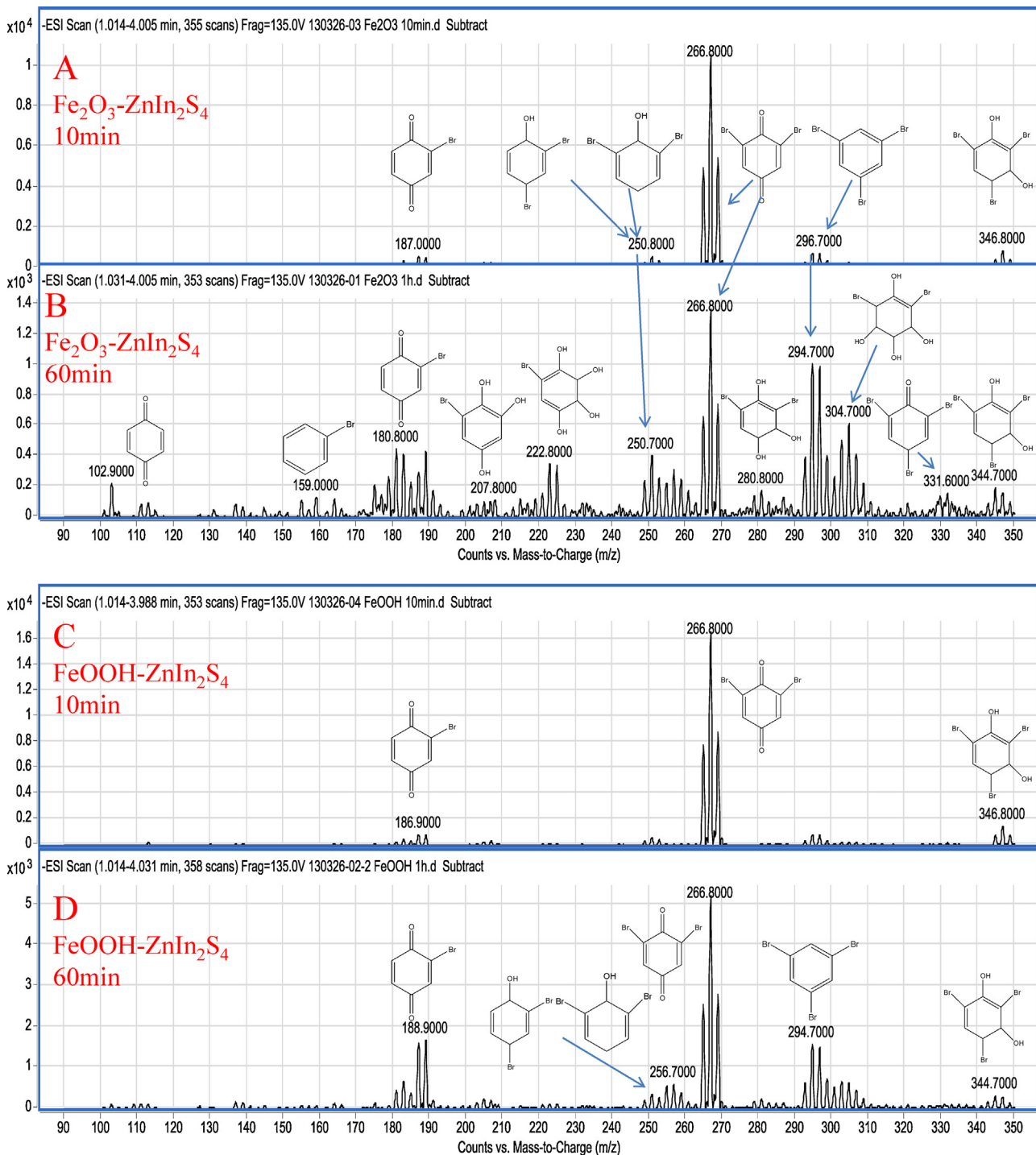
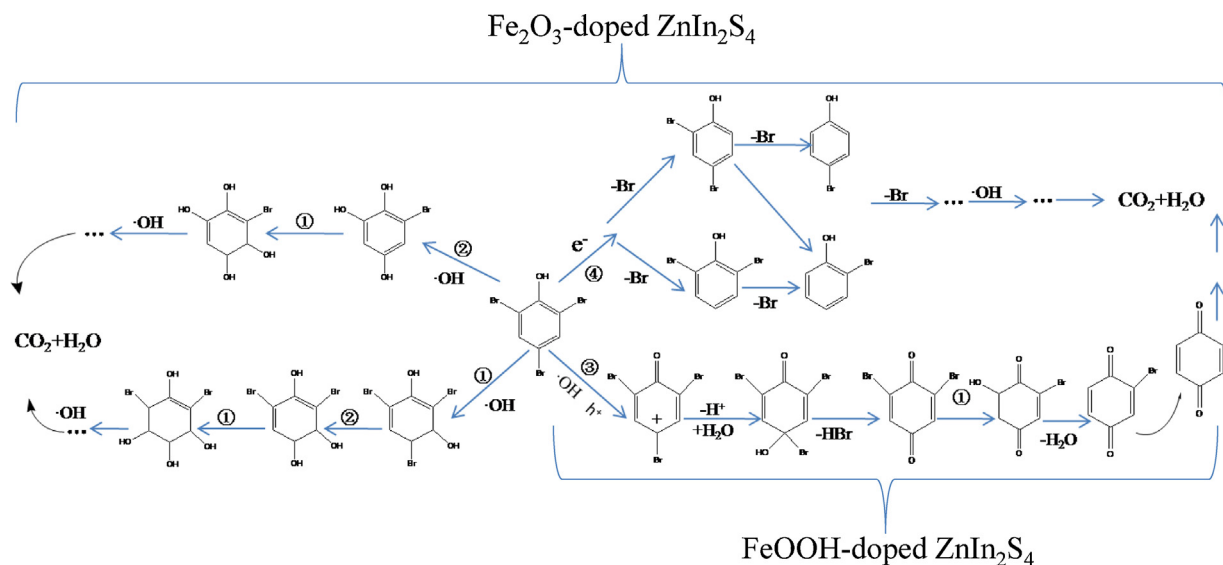


Fig. 9. The intermediate products resulting from 2,4,6-TBP degradation at 10 min and 60 min by Fe₂O₃-ZnIn₂S₄ (A and B) and FeOOH-ZnIn₂S₄ (C and D).

ring by hydroxide radical. The third one (marked as (3)) was the oxidative process through the generated hydroxide radical or the photon-generated holes to produce quinones intermediates. The last and subordinate one (marked as (4)) was reductive debromination by photo-induced electrons to produce less-brominated homologues (DBP or BP). However, from the intermediates, the oxidative degradation through the generated hydroxide radical or the photon-generated holes (pathway (3)) played a leading role and pathway (4) played a minor role in the photocatalytic debromination of 2,4,6-TBP on FeOOH/ZnIn₂S₄. In general, the hydroxyl radical active species played an important role in photocatalytic degradation of 2,4,6-TBP no matter on Fe₂O₃/ZnIn₂S₄ or FeOOH/ZnIn₂S₄.

Herein, the role of hydroxyl radical played in photocatalytic debromination mechanism on Fe₂O₃/ZnIn₂S₄ and FeOOH/ZnIn₂S₄ was further determined by using the radical scavenger. Isopropanol was regarded as the best hydroxyl radical scavenger due to the high-rate reaction with ·OH radical [14]. In this work, the degradation rate of 2,4,6-TBP and the debromination efficiency both decreased (Fig. 10) when 0.26 mol l⁻¹ isopropanol was added into the photocatalytic reaction system containing Fe₂O₃/ZnIn₂S₄ photocatalyst. The obvious inhibitory effect of isopropanol suggested that ·OH radical presented as active species in this reaction solution.

As shown in Fig. 11, there was no obvious decrease in degradation rate and debromination efficiency when isopropanol was



Scheme 1. Schematic reaction pathways of 2,4,6-TBP degradation on Fe_2O_3 -doped ZnIn_2S_4 and FeOOH -doped ZnIn_2S_4 .

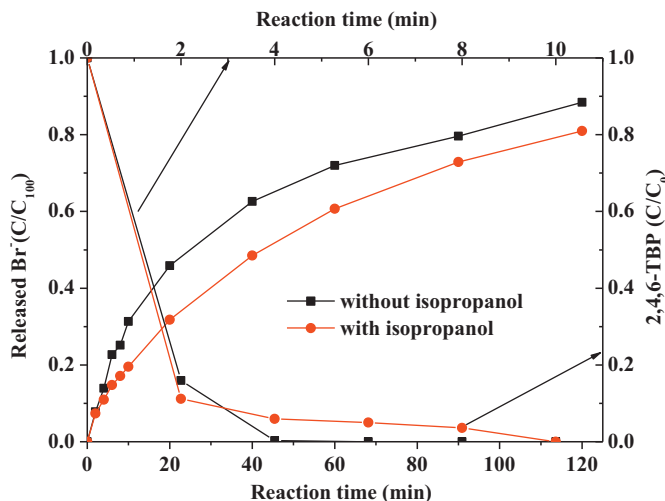


Fig. 10. Effect of isopropanol on the photocatalytic activity of Fe_2O_3 - ZnIn_2S_4 .

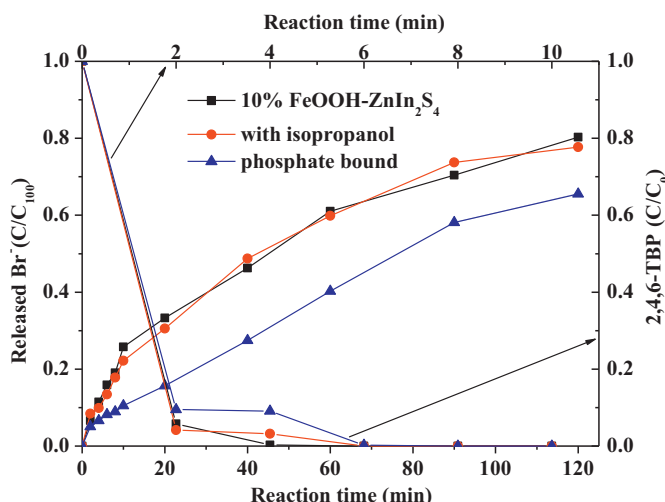
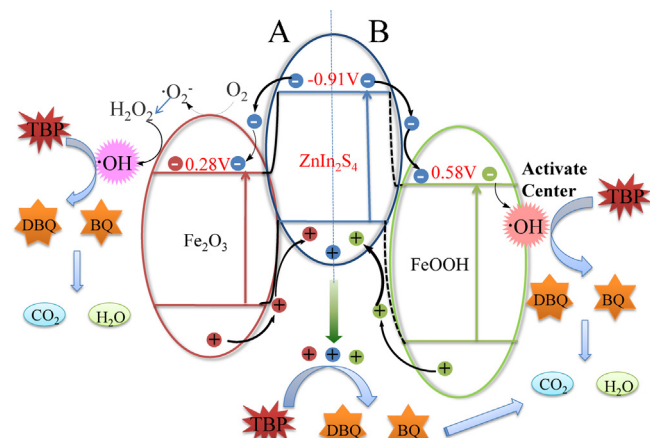


Fig. 11. Effect of isopropanol and phosphate binding on the photocatalytic activity of FeOOH - ZnIn_2S_4 .

added in the presence of $\text{FeOOH}/\text{ZnIn}_2\text{S}_4$, which indicated that $\cdot\text{OH}$ radical was not the main active species in the solution. Previous research [32] had proved that sorption was a critical step for the degradation of organics on FeOOH surface and the highly active radicals were completely consumed on the surface prior to diffusion to the solution. That is to say, the $\cdot\text{OH}$ radicals was consumed on $\text{FeOOH}/\text{ZnIn}_2\text{S}_4$ surface, so the addition of isopropanol did not affect the degradation efficiency. Moreover, another research [23] had implied that surface hydroxyl groups of hydroxylated synthetic α - FeOOH were active sites for promoting $\cdot\text{OH}$ radical generation. In order to further confirm the mechanism, the replacing of the surface hydroxyl groups of FeOOH -doped ZnIn_2S_4 was accompanied by ligand exchange with phosphate due to the strong affinity of phosphate on FeOOH surface [25]. The degradation rate of 2,4,6-TBP and debromination efficiency both decreased in the presence of phosphate bound $\text{FeOOH}/\text{ZnIn}_2\text{S}_4$, which suggested that the hydroxyl groups on FeOOH surface were the active center to generate $\cdot\text{OH}$ radicals.

Based on the results and previous researches, different photocatalytic mechanisms on Fe_2O_3 -doped ZnIn_2S_4 and FeOOH -doped ZnIn_2S_4 were proposed in **Scheme 2**. Adsorption of photons with energy greater than the band gap of photocatalyst resulted in the



Scheme 2. Proposed different photocatalytic degradation mechanisms of Fe_2O_3 - ZnIn_2S_4 (A) and FeOOH - ZnIn_2S_4 (B) (relative band positions calculated versus NHE [4]).

formation of electron–hole pairs. The generated electrons on conduction band of ZnIn_2S_4 immediately transferred to the conduction band of Fe_2O_3 , while the valence band holes of Fe_2O_3 flowed in the opposite direction to the valence band of ZnIn_2S_4 , which effectively reduced the recombination of electron–hole pairs. The accumulated electrons on conduction band of Fe_2O_3 migrated to catalyst surface and reacted with the dissolved oxygen to form $\cdot\text{O}_2^-$ which further generated $\cdot\text{OH}$ radicals. Some of the $\cdot\text{OH}$ radicals attacked 2,4,6-TBP adsorbed on the catalyst surface and some migrated to the solution. The accumulated electrons on conduction band of FeOOH were transformed to $\cdot\text{OH}$ radicals at the active center on FeOOH surface. Because of the excellent adsorption capacity of FeOOH -doped ZnIn_2S_4 , the $\cdot\text{OH}$ radicals were depleted by adsorbed 2,4,6-TBP. On the other hand, the holes accumulated on valence band of ZnIn_2S_4 can be used to directly oxidize the 2,4,6-TBP. The biggest mechanism difference between $\text{Fe}_2\text{O}_3/\text{ZnIn}_2\text{S}_4$ and $\text{FeOOH}/\text{ZnIn}_2\text{S}_4$ was that the reaction between $\cdot\text{OH}$ radicals and 2,4,6-TBP mainly occurred at the active center on the surface of FeOOH -doped ZnIn_2S_4 .

3.5. The comparison of photocatalyst stability

The stability and recyclability of composite photocatalyst under irradiation are important issues related to practical application of photocatalysis. Ferric oxide has very stable corundum structure which is good for the stability of composite. Comparing with ferric oxide, ferric oxy-hydroxide FeOOH has poor thermal stability and becomes dehydrated when heated to 150–200 °C, which is not a problem in this photocatalytic process. It is anticipated that the composite can maintain stability during the long-term operation. In order to evaluate the stability and reuse of composite, the comparison study of debromination efficiency and COD_{Mn} removal efficiency during the 10 cycles experiment was conducted. 2,4,6-TBP was completely removed in each cycle. As shown in Fig. 12, the photocatalytic activity of Fe_2O_3 - ZnIn_2S_4 and FeOOH - ZnIn_2S_4 both decreased a little after 10 cycles. The content of released Br^- began to decrease after the 6th cycle and was still maintained at 80% (~10% decrease) after 10 cycles on Fe_2O_3 - ZnIn_2S_4 . However, the decrease in COD_{Mn} removal occurred from the 3rd cycle and finally resulted in 26% COD_{Mn} decrease. About 10% and 33% decrease in debromination and COD_{Mn} removal was obtained after 10 cycles on FeOOH - ZnIn_2S_4 , which indicated the stability of FeOOH - ZnIn_2S_4 was worse than Fe_2O_3 - ZnIn_2S_4 . There were two reasons for the decrease of stability. The first and the most important one was the loss of photocatalyst during the separation process by centrifugation. 44% (11 mg) and 25% (6.2 mg) of Fe_2O_3 - ZnIn_2S_4 and FeOOH - ZnIn_2S_4 were lost after 10 cycles, respectively, corresponding that about 1.0 mg photocatalyst was lost each cycle. The second reason was the deactivation properties of photocatalysts. The reaction of $\cdot\text{OH}$ radicals and 2,4,6-TBP mainly occurred on the surface of FeOOH - ZnIn_2S_4 , while the adsorption capacity decreased after several cycles which affected the photocatalytic activity. That is why the stability of Fe_2O_3 - ZnIn_2S_4 was better than FeOOH - ZnIn_2S_4 .

The short diffusion length of photo-induced holes is the great limitation for photocatalytic activity of ferric oxide and hydroxide. The recombination of holes and electrons occurred prior to diffusion to the surface for reaction. The combination of ZnIn_2S_4 with Fe_2O_3 can prompt the reverse movement of photo-induced electrons and holes of both semiconductors, which might be the main reason for the stability and photocatalytic activity. In other ways, indium as a rare metal may be saved by incorporation of high content (10–15%) of Fe_2O_3 in ZnIn_2S_4 . For the sake of economy, it is anticipated that maybe ZnIn_2S_4 can be used as a co-catalyst to improve the activity of Fe_2O_3 or FeOOH .

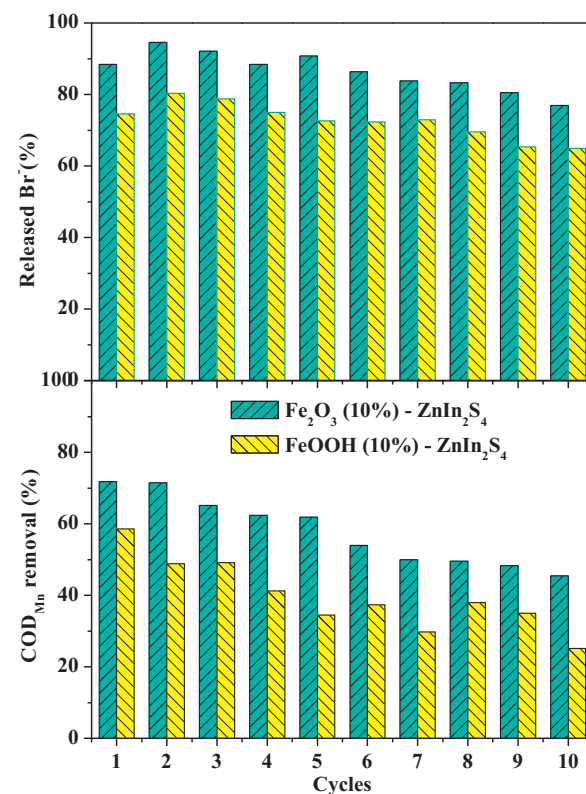


Fig. 12. The stability of Fe_2O_3 - ZnIn_2S_4 and FeOOH - ZnIn_2S_4 by detecting the released Br^- and COD_{Mn} removal during the ten cyclic experiments.

4. Conclusions

Fe_2O_3 and FeOOH doped ZnIn_2S_4 reduced the band gap and increased the degradation efficiency of 2,4,6-TBP comparing with ZnIn_2S_4 both under UV illumination and visible light. According to the degradation rate, debromination and mineralization efficiency, Fe_2O_3 -doped ZnIn_2S_4 exhibited better photocatalytic activity than FeOOH -doped ZnIn_2S_4 . Four main degradation pathways were involved in the photocatalytic degradation of 2,4,6-TBP on Fe_2O_3 -doped ZnIn_2S_4 , which were the hydroxylation process of benzene ring, the substitution reaction of bromide in benzene ring by hydroxide radical, the oxidative process and reductive debromination by photo-induced electrons. While, the oxidative degradation through the generated hydroxide radical or the photon-generated holes played a leading role in the photocatalytic debromination of 2,4,6-TBP on FeOOH - ZnIn_2S_4 .

Appendix A. Supplementary data

Supplementary data associated with this article can be found, in the online version, at <http://dx.doi.org/10.1016/j.apcatb.2013.09.040>.

References

- [1] S. Shen, L. Zhao, Z. Zhou, L. Guo, J. Phys. Chem. C 112 (2008) 16148–16155.
- [2] Z. Lei, W. You, M. Liu, G. Zhou, T. Takata, M. Hara, K. Domen, C. Li, Chem. Commun. (2003) 2142–2143.
- [3] H. Yu, X. Quan, Y. Zhang, N. Ma, S. Chen, H. Zhao, Langmuir 24 (2008) 7599–7604.
- [4] Y. Chen, R. Huang, D. Chen, Y. Wang, W. Liu, X. Li, Z. Li, ACS Appl. Mater. Interfaces 4 (2012) 2273–2279.
- [5] Y. Chen, S. Hu, W. Liu, X. Chen, L. Wu, X. Wang, P. Liu, Z. Li, Dalton Trans. 40 (2011) 2607–2613.
- [6] Y. Xu, M.A.A. Schoonen, Am. Miner. 85 (2000) 543–556.
- [7] J. Bandara, J.A. Mielczarski, A. Lopez, J. Kiwi, Appl. Catal. B: Environ. 34 (2001) 321–333.

- [8] W. Du, Q. Sun, X. Lv, Y. Xu, *Catal. Commun.* 10 (2009) 1854–1858.
- [9] W. Du, Y. Xu, Y. Wang, *Langmuir* 24 (2008) 175–181.
- [10] I.S.X. Pinto, P.H.V.V. Pacheco, J.V. Coelho, E. Lorenccon, J.D. Ardisson, J.D. Fabris, P.P. Souza, K.W.H. Krambrock, L.C.A. Oliveira, M.C. Pereira, *Appl. Catal. B: Environ.* 119/120 (2012) 175–182.
- [11] P. Mazellier, M. Bolte, *J. Photochem. Photobiol. A* 132 (2000) 129–135.
- [12] R. Andreozzi, V. Caprio, R. Marotta, *Water Res.* 37 (2003) 3682–3688.
- [13] Y. Zhao, J. Hu, *Appl. Catal. B: Environ.* 78 (2008) 250–258.
- [14] H. Zhao, Y. Wang, Y. Wang, T. Cao, G. Zhao, *Appl. Catal. B: Environ.* 125 (2012) 120–127.
- [15] X. Qiu, Z. Fang, B. Liang, F. Gu, Z. Xu, *J. Hazard. Mater.* 193 (2011) 70–81.
- [16] J. Zhu, Z. Yin, D. Yang, T. Sun, H. Yu, H.E. Hoster, H.H. Hng, H. Zhang, Q. Yan, *Energy Environ. Sci.* 6 (2013) 987–993.
- [17] S. Krejula, S. Music, *J. Alloys Compd.* 416 (2006) 284–290.
- [18] Y. Nie, C. Hu, J. Qu, X. Zhao, *Appl. Catal. B: Environ.* 87 (2009) 30–36.
- [19] Q. Sun, W. Leng, Z. Li, Y. Xu, *J. Hazard. Mater.* 229/230 (2012) 224–232.
- [20] Y. Shi, H. Li, L. Wang, W. Shen, H. Chen, *Appl. Mater. Interfaces* 4 (2012) 4800–4806.
- [21] D. Bi, Y. Xu, *J. Mol. Catal. A: Chem.* 367 (2013) 103–107.
- [22] M. Pereira, E.M. Garcia, A. Silva, E. Lorencon, J. Ardisson, E. Murad, J. Fabris, T. Matencio, T. Ramalho, M.J. Rocha, *J. Mater. Chem.* 21 (2011) 10280–10282.
- [23] J. He, W. Ma, W. Song, J. Zhao, X. Qian, S. Zhang, J.C. Yu, *Water Res.* 39 (2005) 119–128.
- [24] Y.P. He, Y.M. Miao, C.R. Li, S.Q. Wang, L. Cao, S.S. Xie, G.Z. Yang, B.S. Zou, *Phys. Rev. B* 71 (125411) (2005) 1–9.
- [25] M. Sui, L. Sheng, K. Lu, F. Tian, *Appl. Catal. B: Environ.* 96 (2010) 94–100.
- [26] B. Gao, L. Liu, J. Liu, F. Yang, *Appl. Catal. B: Environ.* 129 (2013) 89–97.
- [27] D. Fu, P.G. Keech, X. Sun, J.C. Wren, *Phys. Chem. Chem. Phys.* 13 (2011) 18523–18529.
- [28] X. Huang, J. Guan, Z. Xiao, G. Tong, F. Mou, X. Fan, *J. Colloid Interface Sci.* 357 (2011) 36–45.
- [29] K. Cheng, C. Liang, *Sol. Energy Mater. Sol. Cells* 94 (2010) 1137–1145.
- [30] M. Li, J. Su, L. Guo, *Int. J. Hydrogen Energy* 33 (2008) 2891–2896.
- [31] S. Chakrabarti, D. Ganguli, S. Chaudhuri, *Physica E* 24 (2004) 333–342.
- [32] T. Zhang, C. Li, J. Ma, H. Tian, Z. Qiang, *Appl. Catal. B: Environ.* 82 (2008) 131–137.